



Published in final edited form as:

MAGMA. 2016 February ; 29(1): 49–58. doi:10.1007/s10334-015-0513-4.

## DCE-MRI of hepatocellular carcinoma: perfusion quantification with Tofts model versus shutter-speed model—initial experience

Guido H. Jajamovich<sup>1</sup>, Wei Huang<sup>2</sup>, Cecilia Besa<sup>1</sup>, Xin Li<sup>2</sup>, Aneela Afzal<sup>2</sup>, Hadrien A. Dyvorne<sup>1</sup>, and Bachir Taouli<sup>1</sup>

<sup>1</sup>Department of Radiology and Translational and Molecular Imaging Institute, Icahn School of Medicine at Mount Sinai, 1470 Madison Avenue, New York, NY 10029, USA

<sup>2</sup>Oregon Health & Science University, Portland, OR, USA

### Abstract

**Objective**—To quantify hepatocellular carcinoma (HCC) perfusion and flow with the fast exchange regime-allowed Shutter-Speed model (SSM) compared to the Tofts model (TM).

**Materials and methods**—In this prospective study, 25 patients with HCC underwent DCE-MRI. ROIs were placed in liver parenchyma, portal vein, aorta and HCC lesions. Signal intensities were analyzed employing dual-input TM and SSM models. ART (arterial fraction),  $K^{\text{trans}}$  (contrast agent transfer rate constant from plasma to extravascular extracellular space),  $v_e$  (extravascular extracellular volume fraction),  $k_{\text{ep}}$  (contrast agent intravasation rate constant), and  $\tau_f$  (mean intracellular water molecule lifetime) were compared between liver parenchyma and HCC, and ART,  $K^{\text{trans}}$ ,  $v_e$  and  $k_{\text{ep}}$  were compared between models using Wilcoxon tests and limits of agreement. Test–retest reproducibility was assessed in 10 patients.

**Results**—ART and  $v_e$  obtained with TM; ART,  $v_e$ ,  $k_e$  and  $\tau_f$  obtained with SSM were significantly different between liver parenchyma and HCC ( $p < 0.04$ ). Parameters showed variable reproducibility (CV range 14.7–66.5 % for both models). Liver  $K^{\text{trans}}$  and  $v_e$ ; HCC  $v_e$  and  $k_{\text{ep}}$  were significantly different when estimated with the two models ( $p < 0.03$ ).

**Conclusion**—Our results show differences when computed between the TM and the SSM. However, these differences are smaller than parameter reproducibilities and may be of limited clinical significance.

### Keywords

MRI; Hepatocellular carcinoma; Liver

---

<sup>✉</sup>Bachir Taouli, bachir.taouli@mountsinai.org.

**Authors' contributions** Protocol/project development: Jajamovich, Huang, Taouli. Data collection: Jajamovich, Besa, Dyvorne. Data analysis: Jajamovich, Besa, Li, Afzal, Dyvorne. Wrote the paper: Jajamovich, Taouli.

**Conflict of interest** The authors declare that they have no conflict of interest.

**Ethical approval** All procedures performed in studies involving human participants were in accordance with the ethical standards of the institutional and/or national research committee and with the 1964 Helsinki declaration and its later amendments or comparable ethical standards.

**Compliance with ethical standards**

**Informed consent** Informed consent was obtained from all individual participants included in the study.

## Introduction

Hepatocellular carcinoma (HCC) is the third leading cause of cancer-related death worldwide [1], and its incidence is increasing in the United States [2]. The growth and progression of histological malignancy of HCC are associated with the formation of new blood vessels [3] which happens through angiogenesis and/or by recruiting proangiogenic bone marrow-derived cells [4]. This capability of sustained angiogenesis is one of the hallmarks of cancer [5, 6]. In order to characterize HCC, the quantification of vascular characteristics of HCC is important. MRI and CT play an important role in HCC diagnosis, staging, and treatment planning [7–13].

Dynamic contrast-enhanced (DCE)-MRI is a non-invasive methodology that allows tissue perfusion quantification. Generally, DCE-MRI consists of acquisition of T1-weighted MR images before, during and after an IV injection of a gadolinium-based contrast agent (CA) and the perfusion quantification is the result of modeling the tracer pharmacokinetics as it distributes through the tissue of interest [14–16]. One of such pharmacokinetic models was introduced by Tofts and Kermode [26–28] (TM: Tofts model). This model has been used to extract vascular permeability characteristics of HCC and to assess response to treatment [18, 22, 23, 29]. The TM has also been modified to allow two inputs in order to estimate liver parenchyma perfusion parameters as the liver has both arterial and venous inputs. The resulting dual input TM is equivalent to the dual-input single compartment model proposed by Materne et al. [19, 20], which had been validated in vivo in an animal model [30] and used for liver fibrosis detection [31–34].

Currently, there is no consensus regarding the pharmacokinetic model that should be used to quantify HCC perfusion parameters [17]. For example, Taouli et al. [18] utilized a dual-input single compartment model, while Sahani et al. [21] used a hybrid model composed of a distributed and compartmental component for the intravascular and extravascular spaces, respectively, to extract perfusion parameters from dynamic CT. Due to the fact that HCC lesions receive their supply mainly from the hepatic artery, single input models have also been used by some investigators [17, 22, 23]. Jarnagin et al. [24] and Yopp et al. [25] used the dual compartment version of the TM to quantify changes after therapy. All these studies have used different analysis methods, showing that the post-processing of HCC and liver perfusion data is not standardized and making comparisons between studies difficult.

The TM has similarities with well-established kinetic models used in nuclear medicine where the tracer is measured directly. However, when used in MRI, the CA is measured indirectly through observing its effect on tissue  $^1\text{H}_2\text{O}$  longitudinal relaxation rate constant,  $R_1$  [35]. The TM is essentially derived from the tracer kinetic model with the assumption of linear relationship between CA concentration and  $R_1$ , equivalent to assuming infinitely fast intercompartmental equilibrium water exchange kinetics [35]. However, this assumption might not hold true when there is significant CA extravasation during CA bolus passage through the tissue of interest [35].

The Shutter-Speed family of DCE-MRI pharmacokinetic models takes into consideration the finite tissue intercompartmental equilibrium water exchange kinetics [35–47], which can

include both transcytolemmal and transendothelial water exchanges. However, the more compartments are taken into account, the more variables need to be included for data modeling [43]. The fast exchange regime (FXR)-allowed Shutter-Speed model (SSM) version is a two-site-exchange model accounting for transcytolemmal water exchange. The FXR introduces only one parameter in addition to the conventional parameters of the TM: the mean intracellular water molecule lifetime,  $\tau_i$ . This version of the SSM has been used to quantify perfusion of breast [48] and prostate cancer [49], but not in the liver. It has been suggested that  $\tau_i$  may reflect cellular metabolic activity [50, 51].

Given that the SSM presumably models the underlying MRI physics more realistically than the TM and that the SSM-unique  $\tau_i$  parameter has the potential to provide metabolic information of HCC, the objective of this initial study was to perform quantitative pharmacokinetic analysis of DCE-MRI data from HCC and non tumorous liver parenchyma using the TM and the FXR SSM version, both adapted to allow for two vascular inputs. In addition, the test–retest reproducibility of DCE-MRI parameters was assessed for both models. A secondary objective was to assess the relationship of HCC perfusion parameters with histopathologic markers.

## Materials and methods

### Subjects

This HIPAA compliant prospective study was funded by the National Cancer Institute (Grant Numbers U01 CA172320 and U01 CA154602), and approved by the Icahn School of Medicine at Mount Sinai Program for the Protection of Human Subjects. Written consent was obtained from all patients prior to the exam. The study included 25 consecutive patients with chronic liver disease and HCC that underwent a DCE-MRI exam at Mount Sinai Hospital. Patients were enrolled from June 2013 to June 2014. Liver diseases were related to the following etiologies: chronic hepatitis C ( $n = 18$ ), chronic hepatitis B ( $n = 5$ ), nonalcoholic steatohepatitis ( $n = 1$ ), and unknown cause ( $n = 1$ ).

10 patients were scanned twice for assessment of test–retest parameter reproducibility with a mean interval of  $5 \pm 3$  days (range 2–11 days) between the two scans (and no interval therapy).

Patients with severe renal dysfunction [estimated glomerular filtration rate (eGFR)  $<30$  ml/min/1.73 m<sup>2</sup>] were excluded from the study in order to minimize the risk of nephrogenic systemic fibrosis [52]. Since portal venous flow can increase postprandially [53], all subjects were asked to fast for 6 h before the MRI study.

### MRI acquisition

Examinations were performed with one of three state-of-the art MRI systems (1.5T Siemens Aera, 3T Siemens Skyra, and 3T Siemens mMR, Erlangen, Germany), each equipped with a multichannel spine and body matrix coil for RF receiving. One patient underwent both examinations in the 3T Siemens Skyra system, 6 patients in the 1.5T Siemens Aera system, and 3 patients had their first exams in the 1.5T Aera System and the second ones in the 3T Siemens mMR system.

Patients were positioned arms up in supine position. In addition to routine clinical sequences used to localize and characterize the liver and liver lesions, the following sequences were acquired:

- Breath-hold axial, coronal and sagittal T2-weighted HASTE sequences to localize the abdominal aorta, portal vein, liver, and HCC tumors.
- T1 mapping: The baseline hepatic T1 value was obtained using a breath-hold Look-Locker sequence [54] before the CA injection during DCE-MRI.
- DCE-MRI of the liver (Table 1): a 3D-FLASH sequence was used in the axial plane to obtain acquisitions before, during and after the injection of a CA bolus at a dose of 0.05 mmol/Kg (gadobenate dimeglumine, Multihance, Bracco) injected at 3 mL/s followed by a 25 mL saline flush using an MR-compatible power injector. The 3D acquisition allowed us to cover the entire liver. 100 time points were acquired with an average temporal resolution of  $2.3 \pm 0.2$  s (range 2.0–3.6 s) and a total acquisition time of ~4 min. Patients were allowed to breath freely.

### Image analysis

Images were processed by observer 1 (GHJ, postdoctoral fellow with 3 years of experience in MR image analysis) supervised by a body MR radiologist (observer 2, BT) with 10 years' experience. HCC lesions were identified in consensus fashion by observers 2 and 3 (CB, a radiologist with 4 years' experience in Body MRI) based on routine sequences including contrast-enhanced T1-weighted images and images taken after the injection of CA. Regions of interest (ROIs) were placed to measure signal intensity (SI) in the abdominal aorta at the level of the celiac axis, the portal vein at the level of the porta hepatis, liver parenchyma and HCC lesions after image coregistration with in-house software implemented in MatLab 2014a (Math-Works, Natick, MA) (Fig. 1). ROIs were placed at one time point and automatically copied to all available DCE time points. Manual correction was used when the copied ROI did not cover the area of interest. The abdominal aorta was used as a surrogate of the hepatic artery as the small size of the latter prevented an accurate measurement. For untreated HCCs, ROIs encompassed the whole lesion in the axial view where the lesion was greater; for treated/partially necrotic lesions, ROIs were placed only in the viable component (identified by observer 3 on contrast-enhanced images). For each patient, only the largest HCC lesion was analyzed as the processing of the lesions is more robust with largest lesions.

### Pharmacokinetic modeling

The mean SI in each ROI was used for pharmacokinetic analysis. The conversion from SI to contrast agent relaxation rate constant was performed by inverting the non-linear relationship given by the SPGR signal equation as described in [54, 55]. The CA is delivered to the liver and the HCC through both the hepatic artery and the portal vein. The two inputs can be added in order to construct a single input with an unknown arterial fraction (ART, %) that needs to be estimated jointly with the perfusion parameters. Specifically, let  $R_{AIF}(t)$  and

$R_{VIF}(t)$  be the relaxation rate constants observed in the arterial and venous input functions, then we define the relaxation rate constant of the input,  $R_I(t)$ , as follows.

$$R_I(t) = \frac{ART}{100} R_{AIF}(t) + \left(1 - \frac{ART}{100}\right) R_{VIF}(t - \tau_{VIF}), \quad (1)$$

where  $0 < ART < 100$  and  $\tau_{VIF}$  is a relative delay between the arterial and venous input functions.

Once this equivalent single input was defined, we converted the relaxation rate constant to CA concentration  $C_I(t)$  assuming linearity, as water exchange across blood cell membrane remains in the fast-exchange-limit condition [35, 36]. The relaxivity of the CA and pre-contrast blood T1 values were obtained from literature ([56, 57], respectively), with values of  $8.1 \text{ L mmol}^{-1} \text{ s}^{-1}$  and  $1480 \text{ ms}$  for the 1.5 T system and  $6.3 \text{ L mmol}^{-1} \text{ s}^{-1}$  and  $1649 \text{ ms}$  for the 3T system. Blood CA concentrations were converted to plasma concentrations using an assumed hematocrit value of 0.45 [58]. The pre-contrast T1 values for the liver parenchyma and HCC lesions were obtained from the T1 map. Then, we made use of the Tofts model for kinetic modeling of DCE-MRI data, given by

$$C_{\text{tissue}}(t) = K^{\text{trans}} \int_0^t C_I(t' - \tau_{IN}) e^{-\frac{K^{\text{trans}}}{v_e}(t-t')} dt' \quad (2)$$

where  $C_{\text{tissue}}(t)$  is the concentration curve observed in the tissue of interest,  $K^{\text{trans}}$  and  $v_e$  are the CA transfer rate constant from the blood plasma into the extravascular and extracellular space (EES) and the EES volume fraction, respectively, and  $\tau_{IN}$  is the relative delay between the equivalent single input and  $C_{\text{tissue}}(t)$ . The CA intravasation rate constant,  $k_{\text{ep}}$ , can be calculated as  $K^{\text{trans}}/v_e$ . The effects of transcytolemmal water exchange are ignored in the TM, and thus  $C_{\text{tissue}}(t)$  was converted from tissue  $R_1(t)$  through a linear relationship:

$$R_1(t) = R_{10} + r_1 C_{\text{tissue}}(t), \quad (3)$$

where  $R_{10}$  is the pre-contrast tissue  $R_1$  (measured through T1 mapping) and  $r_1$  is the CA relaxivity.

We also used the SSM model to fit the DCE-MRI data, given by

$$\begin{aligned}
R_1(t) = & \frac{1}{2} \left[ \left\{ 2R_{1i} + \frac{r_1 K^{\text{trans}}}{v_e} \int_0^t C_I(t' - \tau_{IN}) e^{-\frac{K^{\text{trans}}}{v_e}(t-t')} dt' + \frac{R_{10} - R_{1i} + \frac{1}{\tau_i}}{v_e} \right\} \right. \\
& - \left. \left[ \frac{2}{\tau_i} + \frac{R_{1i} - R_{10} - \frac{1}{\tau_i}}{v_e} - \frac{r_1 K^{\text{trans}}}{v_e} \int_0^t C_I(t' - \tau_{IN}) e^{-\frac{K^{\text{trans}}}{v_e}(t-t')} dt' \right]^2 \right. \\
& \left. + \frac{4(1 - v_e)}{\tau_i^2 v_e} \right]^{1/2}
\end{aligned} \tag{4}$$

where  $R_{1i}$  is the intracellular longitudinal relaxation rate constant [59] and was set to be equal to  $R_{10}$  [43]. In addition to the parameters present in the TM ( $K^{\text{trans}}$ ,  $v_e$  and  $k_{\text{ep}} = K^{\text{trans}}/v_e$ ), the SSM also returns the  $\tau_i$  parameter. Note that for the SSM, we do not need to convert relaxation rate constant time-course to concentration curves, avoiding the use of the linearity assumption.

### Statistical analysis

Estimated perfusion parameters obtained with both the TM and SSM (i.e., ART,  $K^{\text{trans}}$ ,  $v_e$ , and  $k_{\text{ep}}$ ) in HCC tumors and liver were compared using Wilcoxon tests and by determining the Bland–Altman limits of agreement (BALA). The BALA quantifies the agreement by computing the differences for each parameter as estimated with the TM and SSM and by providing the corresponding 95 % confidence intervals [60]. Estimated perfusion parameters were also compared between HCC tumors and liver parenchyma using Wilcoxon tests. Test–retest reproducibility was assessed in 10 patients by computing the coefficient of variation (CV) and BALA. Finally, tumor perfusion parameters were compared between different tumor grades and between tumors with and without microvascular invasion using a Mann–Whitney  $U$  test. The statistical analysis was performed in MatLab 2014a (MathWorks, Natick, MA).

## Results

25 HCC lesions were assessed (mean size 4.3 cm, range 1.4–14.0 cm) in 25 patients. One patient was treated with transcatheter arterial chemoembolization prior to MRI and presented with a partially necrotic HCC (approximately 30 % necrosis).

Histopathologic diagnosis of HCC was available in 15 patients after tumor resection performed an average of 11.5 days (range 4–23 days) after MRI scan. Tumors had the following grade distribution: moderately differentiated ( $n = 11$ ) or poorly differentiated ( $n = 4$ ). 11/15 HCC tumors demonstrated microvascular invasion.

### Reproducibility of estimated perfusion parameters

Perfusion parameters showed variable reproducibilities for both TM and SSM analyses, with CV in the range of 14.7–66.5 %, depending on the parameter (Table 2). In HCC, ART and  $v_e$  estimated with the TM showed better reproducibilities than their SSM counterparts, while

$K^{\text{trans}}$  and  $k_{\text{ep}}$  showed better reproducibilities for the SSM.  $K^{\text{trans}}$  estimated with the SSM was the most reproducible parameter in HCC. Similar CV values were seen for all liver parameters of both models. Hepatic  $\tau_j$  was the perfusion parameter with the best reproducibility and the best BALA.

### Estimated perfusion parameters using the TM and the SSM

HCC parameters  $v_e$  and  $k_{\text{ep}}$  for the TM were significantly greater and lower, respectively, when compared to HCC parameters  $v_e$  and  $k_{\text{ep}}$  for the SSM ( $p < 0.03$ ) (Table 3; Fig. 2). For these parameters, BALAs between models were smaller than the test–retest BALA for both the TM and the SSM, suggesting that the model differences are of limited clinical significance. ART and  $K^{\text{trans}}$  for the TM were not significantly different when compared to their SSM counterparts.

Liver  $K^{\text{trans}}$  and  $v_e$  were significantly higher for the TM when compared to their SSM counterparts ( $p < 0.001$ ). However, the two models displayed good agreement when estimating these two parameters in the liver, as determined by BALA [ $K^{\text{trans}}$  and  $v_e$  had BALAs of agreement of (–41.2, 12.9 %) and (–15.8, –3.8 %), respectively]. These two facts imply a significant but small bias. However, the limits of agreement were smaller than the test–retest parameter BALA (Table 2) for both models and therefore, the observed model differences in the parameters were also assumed to be of limited clinical importance. ART and  $k_{\text{ep}}$  measured in liver were not significantly different when estimated with the two models.

### Comparison between HCC and liver parenchyma

Both the TM and SSM produced parameters with significant differences in HCC when compared to background liver (Table 3). ART was significantly higher while  $v_e$  was significantly lower in HCC tumors compared to liver parenchyma for both models ( $p < 0.001$  and  $p < 0.02$ , respectively).  $k_{\text{ep}}$  was significantly higher in HCC only for the SSM ( $p = 0.04$ ).  $\tau_j$  was significantly higher in HCC when compared to liver parenchyma ( $p = 0.008$ ).  $K^{\text{trans}}$  did not show significant differences for either model. Illustrative parametric maps are shown in Fig. 3.

### Correlation with histopathology

ART using the TM was significantly higher in moderately differentiated HCCs compared to poorly differentiated HCCs ( $p = 0.02$ ) (Fig. 4a), and borderline higher in HCCs with microvascular invasion compared to those without ( $p = 0.05$ ) (Fig. 4b). All other HCC DCE-MRI parameters showed no significant difference between different tumor grades and tumors with and without microvascular invasion ( $p > 0.07$  and  $p > 0.5$ , respectively).

### Discussion

In this study, we estimated HCC and liver pharmacokinetic parameters and their test–retest reproducibility from DCE-MRI studies using two different pharmacokinetic models: the dual input TM and the dual input SSM. We observed variable parameter reproducibilities for both models when patients underwent test–retest scans on different days. We also found

significant differences in certain parameters common to both models, although the observed model differences were smaller than parameter variabilities, suggesting limited clinical impact. Both the TM and the SSM produced parameters significantly different when comparing HCC tumors with liver parenchyma.

In order to reflect more realistic tissue environment, pharmacokinetic models should take into account the intercompartmental water exchange effects. However, when additional physiological activities are considered, the processing becomes more complex with more parameters estimated [43]. For example, the FXR-allowed SSM version used in this study allows for a non-infinitely fast transcytolemmal exchange, modeled by the mean intracellular water molecule lifetime,  $\tau_i$ . This parameter has been suggested to reflect cellular metabolic activity, manifest in ATP-driven membrane transport activity in a yeast suspension study [50]. This observation was further validated in a breast DCE-MRI study [51], demonstrating that changes in  $\tau_i$  are not due to changes in cell sizes but rather changes in energetic metabolism-driven cell membrane water permeability. In our study, we found this parameter to be significantly smaller in the liver parenchyma when compared to HCC lesions, which may be explained by high background metabolic activity in the liver parenchyma [61]. A limitation of this study is the lack of information regarding the metabolic activity of the liver parenchyma and HCC lesions. As the parameter  $\tau_i$  is linked to energetic metabolism, a study using co-registered FDG-PET/MRI could assist in validating  $\tau_i$  as an imaging biomarker of metabolic activity.

When using this version of the SSM, we found no significant differences when estimating liver and HCC ART from the acquired DCE-MRI as compared to the TM. It has been suggested that ART can be used to assess response to local regional therapy in HCC [18]. This implies that both the SSM and TM could be used for estimating ART. The SSM returned smaller  $K^{\text{trans}}$  in the liver and, although not statistically significant, greater  $K^{\text{trans}}$  in HCC tumors than those of the TM. This is consistent with previous breast [43, 48] and prostate [49] studies showing greater SSM  $K^{\text{trans}}$  in malignant tumors when compared to TM  $K^{\text{trans}}$ . Although, the SSM has been used in these breast and prostate studies, it has not been used in liver studies before.

The values of  $K^{\text{trans}}$  for HCC reported in this study are similar to published values. Zhu et al. [22] found a baseline  $K^{\text{trans}}$  distribution for HCC between 1.25 and 2.50  $\text{min}^{-1}$  and  $k_{\text{ep}}$  ranging between 1.5 and 3.0  $\text{min}^{-1}$  using DCE-MRI for 34 patients enrolled in a phase II study of multitargeted kinase inhibitor sunitinib [62]. Hsu et al. [23] reported baseline  $K^{\text{trans}}$  between 0.4 and 4.5  $\text{min}^{-1}$  in 31 patients with advanced HCC treated with sorafenib plus tegafur/uracil that underwent a DCE-MRI examination. DCE-MRI was used by Hsu et al. [29] who reported smaller baseline values of  $K^{\text{trans}}$  of approximately 0.3  $\text{min}^{-1}$ .

Assessing the reproducibility of estimated perfusion parameters is critical for the purpose of evaluating tumor response to treatment. ART has been recently reported to have a CV of 64.1 % in the liver parenchyma [54] which is similar to the values obtained in the current study. The reproducibility of  $K^{\text{trans}}$ ,  $v_e$  and  $k_{\text{ep}}$  was reported to be 29, 9 and 24 %, respectively, for different tumor types [63], including renal cell carcinoma, ovarian serous cystadenocarcinoma, peritoneal carcinoma and leiomyosarcoma. In our study, we allowed



for a dual input model and therefore, more parameters needed to be estimated. This could have potentially contributed to degrade the reproducibility. While the SSM is more complex than the TM and has an extra modeling parameter, the use of the SSM for data analysis did not result in less reproducible parameters and  $\tau_j$  was observed to have good reproducibility in the liver.

In this initial study, we found significant differences in the ART of HCC as estimated with the TM when comparing different tumor grades. In poorly differentiated HCCs, ART was decreased due to possibly increased cell proliferation in the tumor center, resulting in an increase of interstitial pressure and the closure of tumor capillaries [64–66]. ART estimated under the TM was higher in lesions with microvascular invasion. This is expected as the invasion is characteristic feature of progressed HCCs with abnormal unpaired arteries [64]. However, these results are preliminary and need to be further confirmed with a larger patient cohort.

One limitation of this study is the relatively small sample size and the fact that only a small subset of HCC lesions had histopathologic results, which reduces power for HCC characterization for many of the DCE-MRI parameters. Another limitation is due to the fact that patients underwent scans of different magnet strengths (1.5 and/or 3.0 T). Ideally, the resulting pharmacokinetic parameters should be independent of imaging conditions as field strength [67], but in practice that might not be the case and different field strengths could be adding variability. Chen et al. [17] identified the choice of contrast agent molecular properties and the temporal resolution of the acquisition as two parameters that influence the quantification of flow and perfusion with DCE-MRI and proposed acquisitions with high enough temporal resolution of 2–5 s to mitigate variability. In this study, we acquired images with an average temporal resolution of 2.3 s and, in addition, only a small set of patients underwent test–retest scans had their scans at different magnet strengths. Nevertheless, the CVs determined in this study agree with those already published in other studies.

## Conclusion

In conclusion, our initial data showed differences between liver and HCC perfusion when computed with the TM and SSM pharmacokinetic analyses of DCE-MRI data. The parameters obtained with both models show variable test–retest reproducibilities that depend on the parameter, rendering the model differences in the common parameters insignificant clinical impact. Both models can be used to quantify perfusion differences between HCC and liver parenchyma. However, the additional parameter obtained with SSM,  $\tau_j$ , has the potential to provide information about HCC tumor biology, which needs to be better defined in larger study cohorts.

## References

1. Ferlay J, Shin HR, Bray F, Forman D, Mathers C, et al. Estimates of worldwide burden of cancer in 2008: GLOBOCAN 2008. *Int J Cancer*. 2010; 127:2893–2917. [PubMed: 21351269]
2. El-Serag HB, Davila JA, Petersen NJ, McGlynn KA. The continuing increase in the incidence of hepatocellular carcinoma in the United States: an update. *Ann Intern Med*. 2003; 139:817–823. [PubMed: 14623619]

3. Folkman J. Angiogenesis: an organizing principle for drug discovery? *Nat Rev Drug Discov.* 2007; 6:273–286. [PubMed: 17396134]
4. Zhu AX, Duda DG, Sahani DV, Jain RK. HCC and angiogenesis: possible targets and future directions. *Nat Rev Clin Oncol.* 2011; 8:292–301. [PubMed: 21386818]
5. Hanahan D, Weinberg RA. The hallmarks of cancer. *Cell.* 2000; 100:57–70. [PubMed: 10647931]
6. Hanahan D, Weinberg RA. Hallmarks of cancer: the next generation. *Cell.* 2011; 144:646–674. [PubMed: 21376230]
7. Lee JM, Yoon JH, Joo I, Woo HS. Recent Advances in CT and MR Imaging for Evaluation of Hepatocellular Carcinoma. *Liver Cancer.* 2012; 1:22–40. [PubMed: 24159569]
8. Earls JP, Theise ND, Weinreb JC, DeCorato DR, Krinsky GA, et al. Dysplastic nodules and hepatocellular carcinoma: thin-section MR imaging of explanted cirrhotic livers with pathologic correlation. *Radiology.* 1996; 201:207–214. [PubMed: 8816545]
9. Libbrecht L, Bielen D, Verslype C, Vanbeckevoort D, Pirenne J, et al. Focal lesions in cirrhotic explant livers: pathological evaluation and accuracy of pretransplantation imaging examinations. *Liver Transplant.* 2002; 8:749–761.
10. Burrel M, Llovet JM, Ayuso C, Iglesias C, Sala M, et al. MRI angiography is superior to helical CT for detection of HCC prior to liver transplantation: an explant correlation. *Hepatology.* 2003; 38:1034–1042. [PubMed: 14512891]
11. Taouli B, Losada M, Holland A, Krinsky G. Magnetic resonance imaging of hepatocellular carcinoma. *Gastroenterology.* 2004; 127:S144–S152. [PubMed: 15508078]
12. Willatt JM, Hussain HK, Adusumilli S, Marrero JA. MR Imaging of hepatocellular carcinoma in the cirrhotic liver: challenges and controversies. *Radiology.* 2008; 247:311–330. [PubMed: 18430871]
13. Guthrie JA. Cirrhosis and focal liver lesions: MRI findings. *Imaging.* 2013; 22:68887955.
14. Padhani AR. Dynamic contrast-enhanced MRI studies in human tumours. *Br J Radiol.* 1999; 72:427–431. [PubMed: 10505003]
15. Padhani AR. Dynamic contrast-enhanced MRI in clinical oncology: current status and future directions. *J Magn Reson Imaging.* 2002; 16:407–422. [PubMed: 12353256]
16. Parker GJ, Suckling J, Tanner SF, Padhani AR, Revell PB, et al. Probing tumor microvasculature by measurement, analysis and display of contrast agent uptake kinetics. *J Magn Reson Imaging.* 1997; 7:564–574. [PubMed: 9170043]
17. Chen B-B, Shih TT-F. DCE-MRI in hepatocellular carcinoma- clinical and therapeutic image biomarker. *World J Gastroenterol.* 2014; 20:3125. [PubMed: 24695624]
18. Taouli B, Johnson RS, Hajdu CH, Oei MT, Merad M, et al. Hepatocellular carcinoma: perfusion quantification with dynamic contrast-enhanced MRI. *Am J Roentgenol.* 2013; 201:795–800. [PubMed: 24059368]
19. Gill AB, Black RT, Bowden DJ, Priest AN, Graves MJ, et al. An investigation into the effects of temporal resolution on hepatic dynamic contrast-enhanced MRI in volunteers and in patients with hepatocellular carcinoma. *Phys Med Biol.* 2014; 59:3187. [PubMed: 24862216]
20. Orton MR, Miyazaki K, Koh DM, Collins DJ, Hawkes DJ, et al. Optimizing functional parameter accuracy for breath-hold DCE-MRI of liver tumours. *Phys Med Biol.* 2009; 54:2197–2215. [PubMed: 19293470]
21. Sahani DV, Holalkere NS, Mueller PR, Zhu AX. Advanced hepatocellular carcinoma: CT perfusion of liver and tumor tissue—initial experience. *Radiology.* 2007; 243:736–743. [PubMed: 17517931]
22. Zhu AX, Sahani DV, Duda DG, di Tomaso E, Ancukiewicz M, et al. Efficacy, safety, and potential biomarkers of sunitinib monotherapy in advanced hepatocellular carcinoma: a phase II study. *J Clin Oncol.* 2009; 27:3027–3035.
23. Hsu CY, Shen YC, Yu CW, Hsu C, Hu FC, et al. Dynamic contrast-enhanced magnetic resonance imaging biomarkers predict survival and response in hepatocellular carcinoma patients treated with sorafenib and metronomic tegafur/uracil. *J Hepatol.* 2011; 55:858–865. [PubMed: 21338641]
24. Jarnagin WR, Schwartz LH, Gultekin DH, Gönen M, Haviland D, et al. Regional chemotherapy for unresectable primary liver cancer: results of a phase II clinical trial and assessment of DCE-MRI as a biomarker of survival. *Ann Oncol.* 2009; 20:1589–1595. [PubMed: 19491285]

25. Yopp AC, Schwartz LH, Kemeny N, Gultekin DH, Gonen M, et al. Antiangiogenic therapy for primary liver cancer: correlation of changes in dynamic contrast-enhanced magnetic resonance imaging with tissue hypoxia markers and clinical response. *Ann Surg Oncol*. 2011; 18:2192–2199. [PubMed: 21286939]
26. Tofts PS, Kermode AG. Measurement of the blood-brain barrier permeability and leakage space using dynamic MR imaging. I. Fundamental concepts. *Magn Reson Med*. 1991; 17:357–367. [PubMed: 2062210]
27. Tofts PS. Modeling tracer kinetics in dynamic Gd-DTPA MR imaging. *J Magn Reson Imaging*. 1997; 7:91–101. [PubMed: 9039598]
28. Tofts PS, Brix G, Buckley DL, Evelhoch JL, Henderson E, et al. Estimating kinetic parameters from dynamic contrast-enhanced T(1)-weighted MRI of a diffusible tracer: standardized quantities and symbols. *J Magn Reson Imaging*. 1999; 10:223–232. [PubMed: 10508281]
29. Hsu C, Yang TS, Huo TI, Hsieh RK, Yu CW, et al. Vandetanib in patients with inoperable hepatocellular carcinoma: a phase II, randomized, double-blind, placebo-controlled study. *J Hepatol*. 2012; 56:1097–1103. [PubMed: 22245891]
30. Materne R, Smith AM, Peeters F, Dehoux JP, Keyeux A, et al. Assessment of hepatic perfusion parameters with dynamic MRI. *Magn Reson Med*. 2002; 47:135–142. [PubMed: 11754452]
31. Annet L, Materne R, Danse E, Jamart J, Horsmans Y, et al. Hepatic flow parameters measured with MR imaging and Doppler US: correlations with degree of cirrhosis and portal hypertension. *Radiology*. 2003; 229:409–414. [PubMed: 12970464]
32. Hagiwara M, Rusinek H, Lee VS, Losada M, Bannan MA, et al. Advanced liver fibrosis: diagnosis with 3D whole-liver perfusion MR imaging—initial experience. *Radiology*. 2008; 246:926–934. [PubMed: 18195377]
33. Patel J, Sigmund EE, Rusinek H, Oei M, Babb JS, et al. Diagnosis of cirrhosis with intravoxel incoherent motion diffusion MRI and dynamic contrast-enhanced MRI alone and in combination: preliminary experience. *J Magn Reson Imaging*. 2010; 31:589–600. [PubMed: 20187201]
34. Van Beers BE, Materne R, Annet L, Hermoye L, Sempoux C, et al. Capillarization of the sinusoids in liver fibrosis: non-invasive assessment with contrast-enhanced MRI in the rabbit. *Magn Reson Med*. 2003; 49:692–699. [PubMed: 12652540]
35. Yankeelov TE, Rooney WD, Li X, Springer CS Jr. Variation of the relaxographic “shutter-speed” for transcytolemmal water exchange affects the CR bolus-tracking curve shape. *Magn Reson Med*. 2003; 50:1151–1169. [PubMed: 14648563]
36. Li X, Rooney WD, Springer CS Jr. A unified magnetic resonance imaging pharmacokinetic theory: intravascular and extracellular contrast reagents. *Magn Reson Med*. 2005; 54:1351–1359. [PubMed: 16247739]
37. Labadie C, Lee JH, Vetek G, Springer CS Jr. Relaxographic imaging. *J Magn Reson B*. 1994; 105:99–112. [PubMed: 7952937]
38. Landis CS, Li X, Telang FW, Molina PE, Palyka I, et al. Equilibrium transcytolemmal water-exchange kinetics in skeletal muscle in vivo. *Magn Reson Med*. 1999; 42:467–478. [PubMed: 10467291]
39. Landis CS, Li X, Telang FW, Coderre JA, Micca PL, et al. Determination of the MRI contrast agent concentration time course in vivo following bolus injection: effect of equilibrium transcytolemmal water exchange. *Magn Reson Med*. 2000; 44:563–574. [PubMed: 11025512]
40. Springer CS, Rooney WD, Li X. The effects of equilibrium transcytolemmal water exchange on the determination of contrast reagent concentration in vivo. *Magn Reson Med*. 2002; 47:422–424.
41. Quirk JD, Bretthorst GL, Duong TQ, Snyder AZ, Springer CS, et al. Equilibrium water exchange between the intra- and extracellular spaces of mammalian brain. *Magn Reson Med*. 2003; 50:493–499. [PubMed: 12939756]
42. Zhou R, Pickup S, Yankeelov TE, Springer CS Jr, Glickson JD. Simultaneous measurement of arterial input function and tumor pharmacokinetics in mice by dynamic contrast enhanced imaging: effects of transcytolemmal water exchange. *Magn Reson Med*. 2004; 52:248–257. [PubMed: 15282806]

43. Li X, Huang W, Yankeelov TE, Tudorica A, Rooney WD, et al. Shutter-speed analysis of contrast reagent bolus-tracking data: preliminary observations in benign and malignant breast disease. *Magn Reson Med*. 2005; 53:724–729. [PubMed: 15723402]
44. Yankeelov TE, Rooney WD, Huang W, Dyke JP, Li X, et al. Evidence for shutter-speed variation in CR bolus-tracking studies of human pathology. *NMR Biomed*. 2005; 18:173–185. [PubMed: 15578708]
45. Chang E, Li X, Jerosch-Herold M, Priest R, Enestvedt CK, et al. The Evaluation of Esophageal Adenocarcinoma Using Dynamic Contrast-Enhanced Magnetic Resonance Imaging. *J Gastrointest Surg*. 2008; 12:166–175. [PubMed: 17768665]
46. Li X, Springer CS, Jerosch-Herold M. First-pass dynamic contrast-enhanced MRI with extravasating contrast reagent: evidence for human myocardial capillary recruitment in adenosine-induced hyperemia. *NMR Biomed*. 2009; 22:148–157. [PubMed: 18727151]
47. Li X, Huang W, Morris EA, Tudorica LA, Seshan VE, et al. Dynamic NMR effects in breast cancer dynamic-contrast-enhanced MRI. *Proc Natl Acad Sci*. 2008; 105:17937–17942. [PubMed: 19008355]
48. Huang W, Li X, Morris EA, Tudorica LA, Seshan VE, et al. The magnetic resonance shutter speed discriminates vascular properties of malignant and benign breast tumors in vivo. *Proc Natl Acad Sci USA*. 2008; 105:17943–17948. [PubMed: 19004780]
49. Li X, Priest RA, Woodward WJ, Tagge IJ, Siddiqui F, et al. Feasibility of shutter-speed DCE-MRI for improved prostate cancer detection. *Magn Reson Med*. 2013; 69:171–178. [PubMed: 22457233]
50. Zhang Y, Poirier-Quinot M, Springer CS Jr, Balschi JA. Active trans-plasma membrane water cycling in yeast is revealed by NMR. *Biophys J*. 2011; 101:2833–2842. [PubMed: 22261073]
51. Springer CS Jr, Li X, Tudorica LA, Oh KY, Roy N, et al. Intratumor mapping of intracellular water lifetime: metabolic images of breast cancer? *NMR Biomed*. 2014; 27:760–773. [PubMed: 24798066]
52. US Food and Drug Administration. Public health advisory: gadolinium-containing contrast agents for magnetic resonance imaging (MRI) -Omniscan, OptiMARK, Magnevist, ProHance, and MultiHance. Department of Health and Human Services. 2013
53. Jajamovich GH, Dyvorne H, Donnerhack C, Taouli B. Quantitative liver MRI combining phase contrast imaging, elastography, and DWI: assessment of reproducibility and postprandial effect at 3.0 T. *PLoS ONE*. 2014; 9:e97355. [PubMed: 24840288]
54. Aronhime S, Calcagno C, Jajamovich GH, Dyvorne HA, Robson P, et al. DCE-MRI of the liver: effect of linear and nonlinear conversions on hepatic perfusion quantification and reproducibility. *J Magn Reson Imaging*. 2014; 40:90–98. [PubMed: 24923476]
55. Schabel MC, Parker DL. Uncertainty and bias in contrast concentration measurements using spoiled gradient echo pulse sequences. *Phys Med Biol*. 2008; 53:2345. [PubMed: 18421121]
56. Pintaske J, Martirosian P, Graf H, Erb G, Lodemann KP, et al. Relaxivity of Gadopentetate Dimeglumine (Magnevist), Gadobutrol (Gadovist), and Gadobenate Dimeglumine (Multi-Hance) in human blood plasma at 0.2, 1.5, and 3 Tesla. *Invest Radiol*. 2006; 41:213–221. [PubMed: 16481903]
57. Zhang X, Petersen ET, Ghariq E, De Vis JB, Webb AG, et al. In vivo blood T(1) measurements at 1.5 T, 3 T, and 7 T. *Magn Reson Med*. 2013; 70:1082–1086. [PubMed: 23172845]
58. Cuenod CA, Balvay D. Perfusion and vascular permeability: basic concepts and measurement in DCE-CT and DCE-MRI. *Diagn Interv Imaging*. 2013; 94:1187–1204. [PubMed: 24211260]
59. Huang W, Li X, Chen Y, Li X, Chang MC, et al. Variations of dynamic contrast-enhanced magnetic resonance imaging in evaluation of breast cancer therapy response: a multicenter data analysis challenge. *Transl Oncol*. 2014; 7:153–166. [PubMed: 24772219]
60. Altman, DG. *Practical statistics for medical research*. Boca Raton: CRC Press; 1990.
61. Okazumi S, Isono K, Enomoto K, Kikuchi T, Ozaki M, et al. Evaluation of liver tumors using fluorine-18-fluorodeoxyglucose PET: characterization of tumor and assessment of effect of treatment. *J Nucl Med*. 1992; 33:333–339. [PubMed: 1311035]
62. Papaetis GS, Syrigos KN. Sunitinib: a multitargeted receptor tyrosine kinase inhibitor in the era of molecular cancer therapies. *BioDrugs*. 2009; 23:377–389. [PubMed: 19894779]

63. Galbraith SM, Lodge MA, Taylor NJ, Rustin GJ, Bentzen S, et al. Reproducibility of dynamic contrast-enhanced MRI in human muscle and tumours: comparison of quantitative and semi-quantitative analysis. *NMR Biomed.* 2002; 15:132–142. [PubMed: 11870909]
64. Choi JY, Lee JM, Sirlin CB. CT and MR imaging diagnosis and staging of hepatocellular carcinoma: part I. Development, growth, and spread: key pathologic and imaging aspects. *Radiology.* 2014; 272:635–654. [PubMed: 25153274]
65. Asayama Y, Yoshimitsu K, Irie H, Nishihara Y, Aishima S, et al. Poorly versus moderately differentiated hepatocellular carcinoma: vascularity assessment by computed tomographic hepatic angiography in correlation with histologically counted number of unpaired arteries. *J Comput Assist Tomogr.* 2007; 31:188–192. [PubMed: 17414751]
66. El-Assal ON, Yamanoi A, Soda Y, Yamaguchi M, Igarashi M, et al. Clinical significance of microvessel density and vascular endothelial growth factor expression in hepatocellular carcinoma and surrounding liver: possible involvement of vascular endothelial growth factor in the angiogenesis of cirrhotic liver. *Hepatology.* 1998; 27:1554–1562. [PubMed: 9620326]
67. Tofts PS. T1-weighted DCE imaging concepts: modelling, acquisition and analysis. *MAGNETOM Flash.* 2010:30–39.

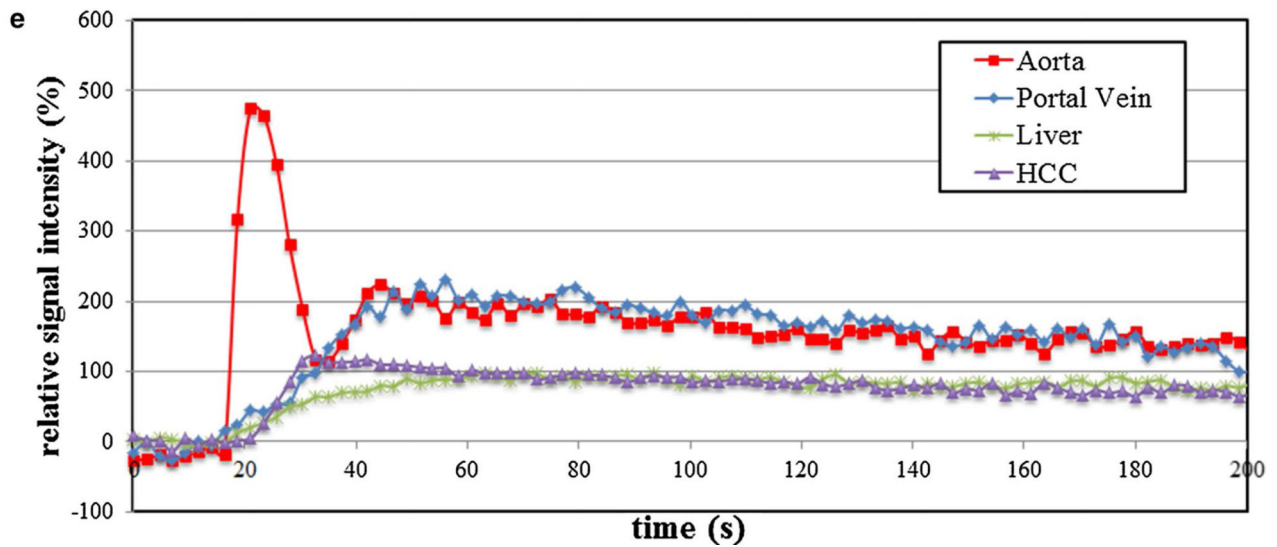
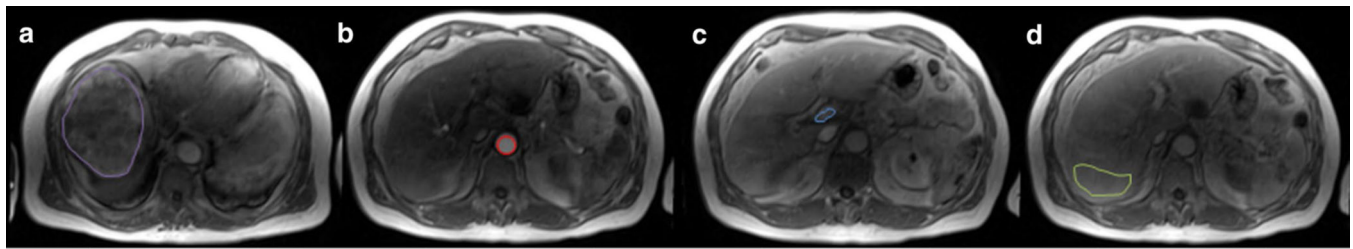


**Fig. 1.** 66 year old male patient with large HCC in the right hepatic lobe (13 cm). Axial DCE-MR images acquired using 3D-FLASH sequence at 1.5T (TR/TE/FA 2.74/1.09/11.5°, matrix 192 × 106, slice thickness 4 mm, acceleration factor 3, 44 slices, 100 time points with temporal resolution of 2.02 s) demonstrate ROI placement in different regions at different time points: tumor (*purple*) acquired at 20 s post injection (**a**), abdominal aorta (*red*) (**b**, 11 s post injection), main portal vein (*blue*) (**c**, 28 s post injection), and liver parenchyma (*green*) (**d**, 55 s post injection). Plots below **e** demonstrate relative signal intensity versus time curve [y axis:  $100 \times (SI/SI_0 - 1)$ , with SI and  $SI_0$  representing the signal intensity and signal intensity before enhancement, respectively]. Plot shows fast enhancement and subsequent washout of HCC as opposed to slow enhancement of liver parenchyma

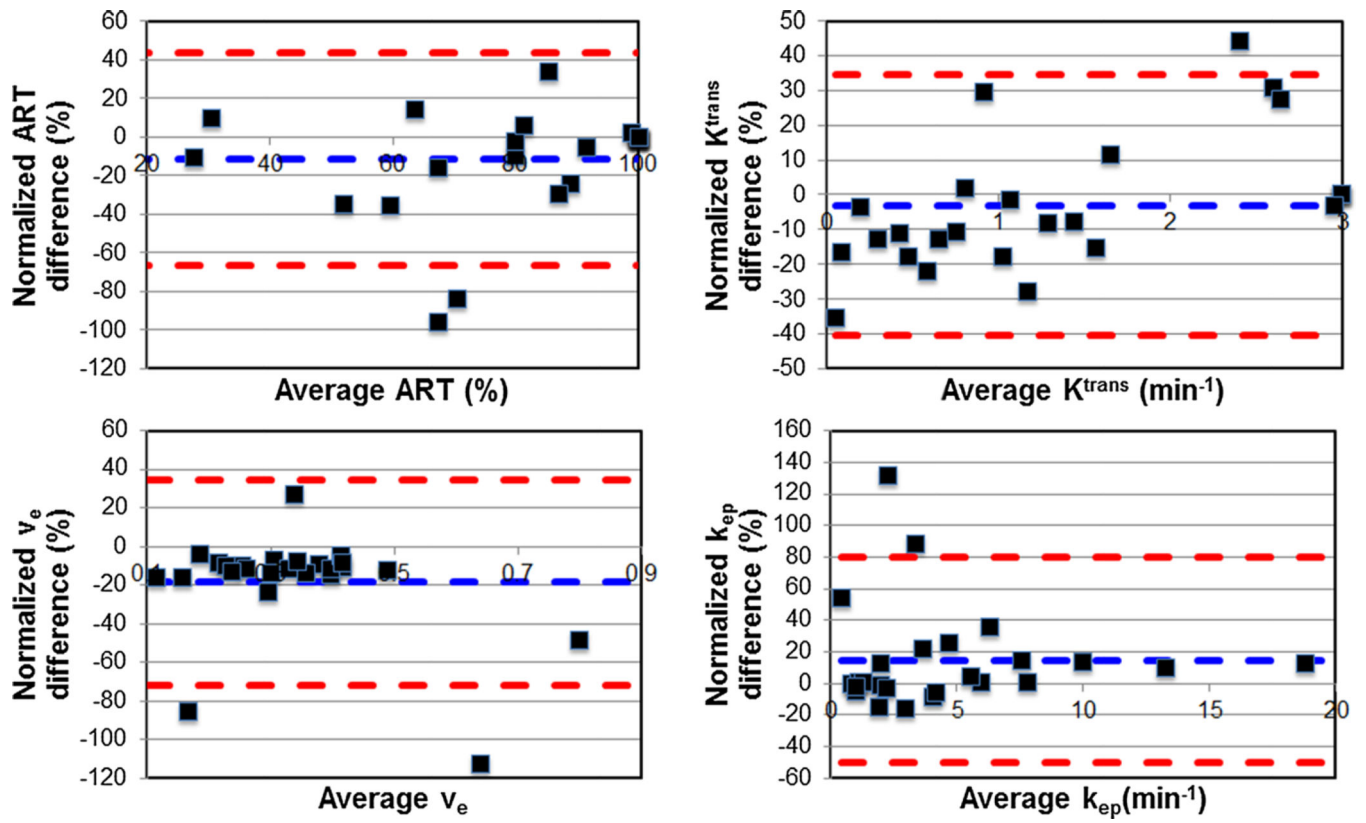


**Fig. 2.** Bland–Altman plots show the comparison of HCC perfusion parameters obtained with Tofts and Shutter-Speed models (differences were normalized by average parameter values). Resulting Bland–Altman limits of agreement (*red dash line*) are smaller than Bland-Altman limits of agreement for test–retest variability (see also Tables 2 and 3)

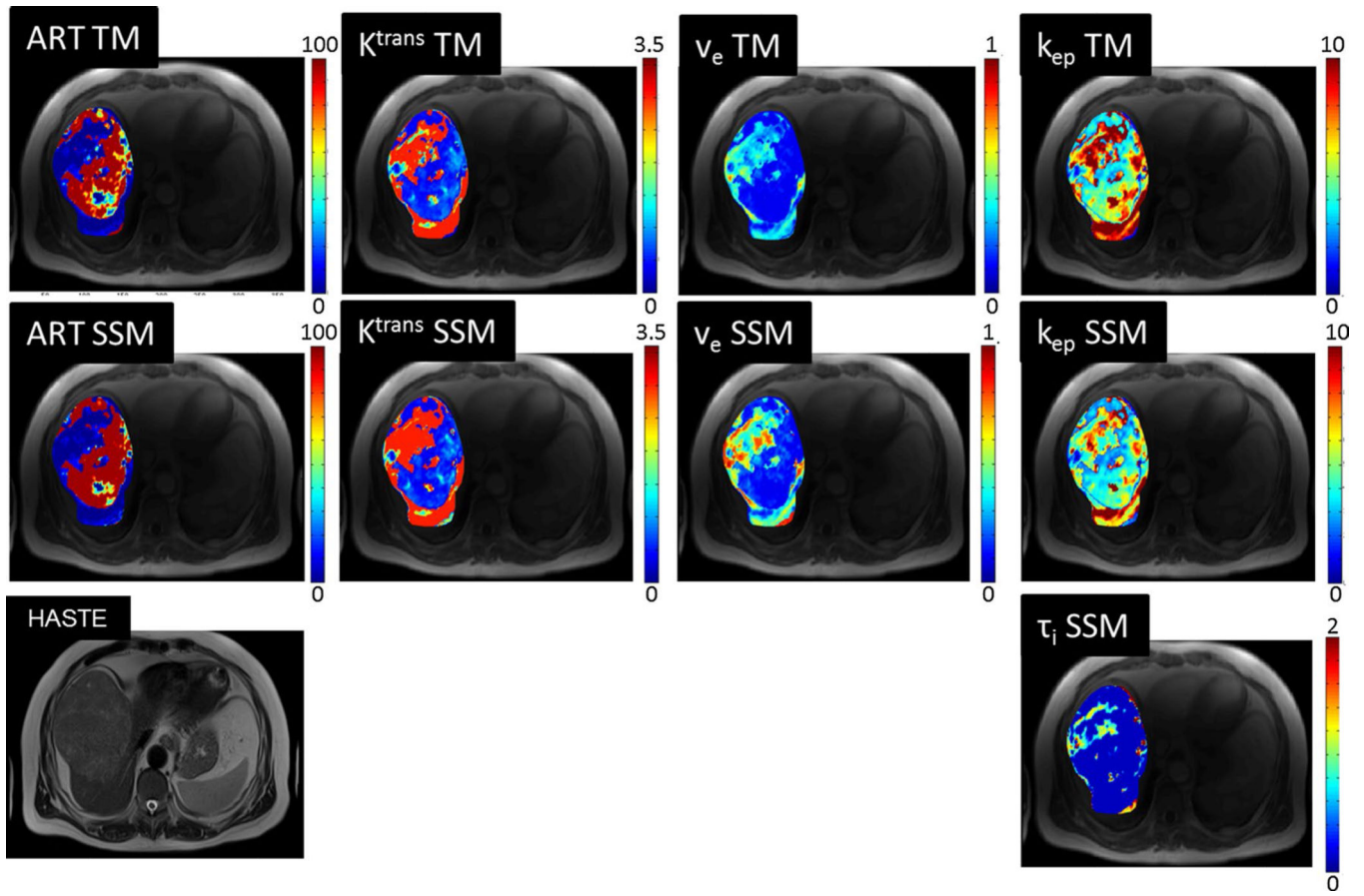


**Fig. 3.** Axial T2 HASTE, and DCE-MRI parametric maps for same patient as in Fig. 1. Regional differences in the tumor and differences between HCC and background liver parenchyma are visually identified. Estimated perfusion parameters from mean ROI signal intensity for HCC/liver were: for Tofts model, ART 100 %/28 %,  $K^{\text{trans}}$  1.1/1.9  $\text{min}^{-1}$ ,  $v_e$  0.3/0.7, and  $k_{\text{ep}} = 4.2/2.5 \text{ min}^{-1}$ ; for Shutter-Speed model, ART 100 %/31 %,  $K^{\text{trans}}$  1.0/1.8  $\text{min}^{-1}$ ,  $v_e$  0.3/0.7,  $k_{\text{ep}}$  3.8/2.4  $\text{min}^{-1}$ , and  $\tau_i$  0.1/0.1 s



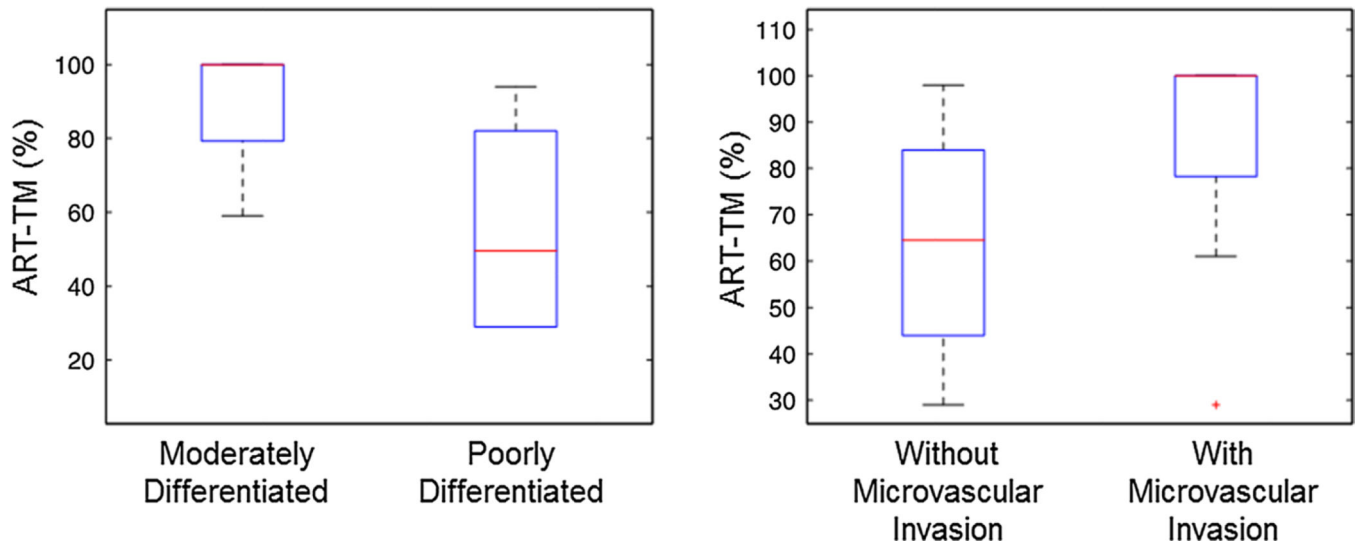


**Fig. 4.**  
*Box plot* distributions of HCC ART measured with Tofts model analysis of DCE-MRI data, in relation to histopathologic parameters in 17 patients with 17 tumors (tumor grade and presence of microvascular invasion)

Author Manuscript

Author Manuscript

Author Manuscript

Author Manuscript

**Table 1**

## DCE-MRI pulse sequence parameters

Scanner	1.5T <sup>a</sup> (n = 26)	3.0T <sup>b</sup> (n = 6)	3.0T <sup>c</sup> (n = 3)
Sequence type	3D GRE (FLASH)	3D GRE (FLASH)	3D GRE (FLASH)
Orientation	Axial	Axial	Axial
Repetition time (ms)	2.74	2.69	2.71
Echo time (ms)	1.09	0.98	0.98
Flip Angle	11.5	11.5	11
Field of view (mm <sup>2</sup> )	370 × 250	370 × 260–280	400 × 300
Acquisition matrix	192 × 106	192 × 107	192 × 115
Slice thickness (mm)	4	4	4.5
Number of slices	44	44	44
Acceleration <sup>d</sup>	R = 3	R = 2	R = 2
Acquisition time	202.4 ± 0.4 s	246.4 ± 50.3	361

<sup>a</sup>Siemens Aera;

<sup>b</sup>Siemens Skyra;

<sup>c</sup>Siemens mMR GRE: gradient echo,

<sup>d</sup>using CAIPIRINHA: Controlled Aliasing in Parallel Imaging Results in Higher Acceleration

**Table 2**

Coefficients of variation (mean and range %) and Bland–Altman limits of agreement (BALA %) for DCE-MRI parameters obtained with the Tofts model (TM) and the shutter-speed model (SSM) in the test–retest study ( $n = 10$ )

Parameter	Model	Liver	HCC
ART	TM		
	CV (%)	63.3 (4.9–137.2)	31.4 (0.0–138.6)
	BALA (%)	–267.6, 185.1	–152.9, 155.6
	SSM		
	CV (%)	66.5 (8.5–141.4)	54.9 (0.0–141.4)
	BALA (%)	–273.4, 185.2	–229.5, 198.1
$K^{\text{trans}}$	TM		
	CV (%)	47.1 (0.0–112.9)	28.9 (0.0–82.9)
	BALA (%)	–136.1, 174.8	–105.7, 134.8
	SSM		
	CV (%)	46.5 (0.1–113.5)	25.1 (0.0–94.9)
	BALA (%)	–144.4, 175.2	–119.2, 126.5
$v_e$	TM		
	CV (%)	37.9 (0.4–79.5)	36.3 (0.0–89.4)
	BALA (%)	–86.3, 139.9	–98.0, 158.9
	SSM		
	CV (%)	39.4 (1.5–74.1)	50.8 (2.0–93.1)
	BALA (%)	–89.1, 143.6	–106.2, 191.9
$k_{ep}$	TM		
	CV (%)	34.4 (3.2–87.9)	44.1 (3.3–82.9)
	BALA (%)	–128.9, 124.3	–160.3, 123.4
	SSM		
	CV (%)	32.2 (2.2–88.2)	38.2 (2.2–65.2)
	BALA (%)	–130.6, 117.5	–132.6, 47.3
$\tau_i$	SSM		
	CV (%)	14.7 (0.0–55.9)	42.6 (0.0 – 130.5)
	BALA (%)	–69.4, 81.6	–206.1, 161.5

ART arterial fraction (%),  $K^{\text{trans}}$  CA transfer rate constant from the blood plasma into the extravascular and extracellular space ( $\text{min}^{-1}$ ),  $v_e$  extravascular and extracellular space volume fraction,  $k_{ep}$  CA intravasation rate constant ( $\text{min}^{-1}$ ),  $\tau_i$ : mean intracellular water molecule lifetime (s)

**Table 3**

Estimated liver and HCC perfusion parameters (mean  $\pm$  SD) using Tofts model (TM) and shutter-speed model (SSM) in 25 patients with 25 HCCs

Parameter	Model	Liver	HCC	p <sup>*</sup>
ART	TM	40.12 $\pm$ 26.75	85.12 $\pm$ 21.71	<b>&lt;0.001</b>
	SSM	42.36 $\pm$ 27.17	77.44 $\pm$ 25.78	<b>&lt;0.001</b>
	<i>p</i> <sup>**</sup>	0.08	0.07	
	CV	12.5 (0.0–64.3)	11.7 (0.0–68.1)	
	BALA	–39.9, 55.7	–66.5, 43.8	
$K^{\text{trans}}$	TM	1.21 $\pm$ 0.63	1.34 $\pm$ 0.96	0.59
	SSM	1.05 $\pm$ 0.58	1.39 $\pm$ 1.09	0.26
	<i>p</i> <sup>**</sup>	<b>&lt;0.001</b>	0.39	
	CV	10.12 (0.1–39.0)	10.4 (0.0–31.2)	
	BALA	–41.2, 12.9	–40.5, 34.3	
$v_e$	TM	0.44 $\pm$ 0.14	0.37 $\pm$ 0.21	<b>0.02</b>
	SSM	0.40 $\pm$ 0.13	0.30 $\pm$ 0.12	<b>0.004</b>
	<i>p</i> <sup>**</sup>	<b>&lt;0.001</b>	<b>&lt;0.001</b>	
	CV	6.9 (0.3–11.2)	14.5 (3.0–79.4)	
	BALA	–15.8, –3.8	–71.5, 34.7	
$k_{ep}$	TM	2.92 $\pm$ 1.59	4.25 $\pm$ 4.11	0.13
	SSM	2.75 $\pm$ 1.48	4.88 $\pm$ 4.60	<b>0.04</b>
	<i>p</i> <sup>**</sup>	0.16	<b>0.03</b>	
	CV	5.3 (0.0–28.5)	13.7 (0.0–92.7)	
	BALA	–28.3, 19.5	–50.0, 79.6	
$\tau_i$	SSM	0.11 $\pm$ 0.02	0.29 $\pm$ 0.53	<b>0.008</b>

Coefficients of variation (mean and range %) and Bland–Altman limits of agreement (BALA %) obtained for DCE-MRI parameters obtained with both models

ART arterial fraction (%),  $K^{\text{trans}}$  CA transfer rate constant from the blood plasma into the extravascular and extracellular space ( $\text{min}^{-1}$ ),  $v_e$  extravascular and extracellular space volume fraction,  $k_{ep}$  CA intravasation rate constant ( $\text{min}^{-1}$ ),  $\tau_i$ : mean intracellular water molecule lifetime (s)

\* *p* value computed using a Wilcoxon test when comparing a parameter in the liver parenchyma versus HCC;

\*\* *p* value computed using a Wilcoxon test when comparing a parameter common to the TM and the SSM in a given tissue